

# MEASUREMENTS OF FLOW VELOCITY AND SCALAR CONCENTRATION IN TURBULENT MULTI-COMPONENT JETS

Soleimani nia, M.<sup>1</sup>, Maxwell, B.M.<sup>1</sup>, Oshkai, P.<sup>1</sup>, and Djilali, N.<sup>1</sup>

<sup>1</sup>Institute for Integrated Energy Systems, University of Victoria,  
PO Box 1700 STN CSC, Victoria BC, V8W 2Y2, Canada, majids@uvic.ca

## ABSTRACT

Development of modern safety standards for hydrogen infrastructure requires fundamental insight into the physics of buoyant gas dispersion into ambient air, from realistic flow geometries. In the present study, inert compressible air and helium releases from a round opening in a curved pipe were considered, experimentally. Particle Image Velocimetry (PIV) and Planar Laser-Induced Fluorescence (PLIF) techniques were employed simultaneously to provide instantaneous and time-averaged patterns of flow velocity and gas concentrations. A range of gas densities and Reynolds numbers were considered in order to quantify their effects on the resulting flow structure. Significant differences were found between the spreading rate of round jets and those considered here. The findings indicate that use of conventional round jet assumptions are inadequate to predict gas concentration, entrainment rates and, consequently, the extent of the flammability envelope of the gas leak.

## 1.0 INTRODUCTION

Worldwide attempts continue to improve renewable energy technologies as an alternative for traditional power supply in the energy grid. Hydrogen, as one of the renewable energy vectors, can burn or react with almost no pollution. Commonly, it is used in electrochemical cells (fuel cells) to power vehicle and electrical devices, but can also be burned directly in engines. It can also be used as a key solution to renewable energy storage. However, modern safety standards for hydrogen infrastructure must be assured before widespread public use can become possible. To inform the development of these new standards, the current study focuses on obtaining detailed velocity and concentration data, to characterize the effect of jet exit conditions on hydrogen dispersion from realistic geometries. The aim is to better understand the flow structures and flammability regions associated with hydrogen outflow from pipelines. As a result, the knowledge of explosive limits of hydrogen, and the flammable envelope surrounding the site of an uncontrolled hydrogen release, can thus be estimated from the concentration field. These comprehensive experimental data sets would also serve to validate detailed numerical investigations.

Depending on system pressures and velocity, fuel leaks can be subsonic, sonic or supersonic. Jets can also be dominated by buoyancy or momentum. Jets issuing through round holes from flat surfaces have received the most attention in previous investigations due to the well-known axi-symmetric nature and self-similarity of flow. In general, one can categorize a round jet nozzle type as a sharp-edged orifice plate (OP), smooth contraction (SC), or a long pipe (LP). Among these three different nozzles, the most research was performed on SC nozzles [1, 2]. It has been shown that such SC jets have a nearly laminar flow profile at the jet exit with a uniform ‘top-hat’ velocity profile. LP nozzles [3, 4, 5], on the other hand, produce a nearly gaussian velocity profile due to the fully-developed turbulence within the pipe. Sharp-edged OP jets have received more recent attention, in the last decade, where detailed measurements [6, 7] have revealed that this configuration has the highest mixing rates downstream from the release nozzle. It is noteworthy that all aforementioned studies, as well as related previous investigations on round jets, have been limited to leaks through flat surfaces, where the direction of the jet mean flow was aligned with the flow origin. While the information contained in such studies has contributed to the knowledge base on round axi-symmetric jets, they do not address the gas dynamic evolution and turbulent mixing from realistic piping arrangement.

In the current study, a physically realistic and novel configuration is considered. Here, the jet evolution through a round 2 mm diameter hole ( $D=2$  mm), which has been machined on the side of a 6.35 mm diameter tube, is studied. The resulting jet flow is thus perpendicular to the mean flow inside of the tube. From now on, we refer to this jet configuration as a 3D jet. This permits the measurement of flow velocity and concentration fields for a practical scenario in order to compare with previous investigations of leaks through flat surfaces. The purpose is to identify and characterize departures from standard axis-symmetric jet conditions, and to provide a complete database for the validation of CFD models to cover a range of conditions which are found in hypothetical, yet realistic accidental leakage scenarios. Air and helium jets were both considered, in order to provide insight on the effect of buoyancy and Reynolds numbers on the jet evolution. Also, due to its low density, helium was used as a substitute for hydrogen to study the inert dispersion resulting from the jet. Particle Imaging Velocimetry (PIV) and acetone-seeded Planar Laser-Induced Fluorescence (PLIF) was used to measure the high-resolution instantaneous spatial distribution of velocity and concentration, respectively. To compare further the 3D jet results with axis-symmetric jets, measurements are also carried out on the same diameter hole through an OP type flat surface jet. All results are provided with up to 13 diameters from the jet orifice, in order to focus on the near-field region.

## 2.0 METHODOLOGY

### 2.1 Experimental Facility

The experiments were conducted within a controlled environment, with minimal ambient air flow and consistent room temperature ( $\sim 22^\circ$ ). Dry filtered air was supplied by a central flow facility while pure scientific grade helium was supplied through compressed T-cylinders, both at  $\pm 1^\circ$  of the room temperature. The gases were first transmitted through mass flow controllers (Bronkhorst, EL-FLOW series) in order to provide a controlled mass flow rate to the system. The gases were then passed through the PIV seeder (LaVision Aerosol Generator). The gases were seeded by Di-Ethyl-Hexyl-Sebacate (DEHS) particles, with a typical diameter of less than 1  $\mu\text{m}$ . Afterwards, the gas passed through two designed atomizers, to mix with acetone vapor as a molecule tracer for PLIF. All mixing procedures were controlled by mass flow controllers. Also, the mixing was monitored by pressure transducers and thermocouples at different locations within the system. After the gas was mixed and seeded with the PIV and PLIF tracers, the flow entered the test section of the tube. Figure 1 shows the schematic of the jet flow evolution from the tube. Measurements were obtained on two different planes. These planes are notably the  $YZ$  plane (perpendicular to direction of mean flow inside the tube) and the  $XZ$  plane (parallel to tube's mean flow direction). The configuration therefore provides some insight into the three-dimensionality of jet flow. Measurements are thus taken along the jet centerline, and on lines which are normal to the centerline. It is worth noting that the potential exists for the jet centerline to deviate from the orifice axis ( $Z$ -axis). The jet centerline and normal lines are shown as  $s$  and  $n$  coordinates in Fig. 1, respectively. Distances reported here have been normalized such that

$$X = \frac{x}{D}, \quad Y = \frac{y}{D}, \quad Z = \frac{z}{D} \quad (1)$$

where  $D$ , the diameter of the orifice, is taken as a reference length scale. In order to compare the two different gas flows, the initial averaged momentum flux ( $\langle M_j \rangle_{\text{flux}}$ ) at the jet exit was matched, as suggested in [8, 2]. This matching was achieved, through trial and error, by varying the gas volumetric flow rate ( $Q$ ) in the system to obtain the desired average jet velocity ( $\langle V_j \rangle$ ). Here, the initial average  $\langle M_j \rangle_{\text{flux}}$  was calculated based on time-averaged jet velocity  $\langle V_j \rangle$  measured at closest vertical distance,  $Z \simeq 0$ , to the orifice exit by using

$$\langle M_j \rangle_{\text{flux}} = \int_{Z \simeq 0} \rho_j \langle V_j \rangle^2 dA = \rho_j \langle V_j \rangle^2 D^2 \quad (2)$$

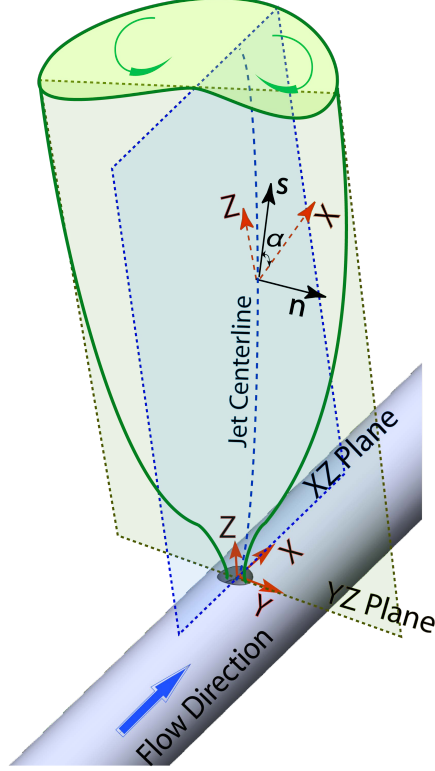


Figure 1: Schematic of the 3D jet flow experiment

where the subscript 'j' refers to the conditions at the nozzle. The term  $\frac{1}{4}\pi$  in the orifice area has been neglected for simplicity and also to conform the previous studies [8]. Table 1 shows the flow parameters and properties used in this study, for both the 3D and OP jet configurations. Fluids properties have been evaluated at equimolar conditions using data obtained from NASA [9].

Table 1: Flow properties

Jet	$Q$ [L/min]	$\langle V_j \rangle_{max}$ [m/s]	$\rho_j$ [Kg/m <sup>3</sup> ]	$\langle \nu \rangle$ [m <sup>2</sup> /s]	$\langle M_j \rangle_{flux}$ [N]	$Re$	$Fr$
3D Air	15	147.5	1.17	$1.59 \times 10^{-5}$	0.1018	18554	N/A
OP Air	15	127.6	1.17	$1.59 \times 10^{-5}$	0.0762	16050	N/A
3D He	35	399.7	0.164	$1.91 \times 10^{-5}$	0.1048	41853	1144
OP He	35	341.9	0.164	$1.91 \times 10^{-5}$	0.0767	35801	978

## 2.2 Velocity Measurements

Particle Imaging Velocimetry (PIV) was used to capture two-dimensional velocity flow field information. A light sheet was created by a pulsed laser, which illuminated a two-dimensional cross-section of the seeded flow. Scattered light from the tracer particles was recorded by a charge-coupled device (CCD) camera at two different times. Displacements of particles were then measured in the field. Thus, the corresponding velocity components were calculated in each direction.

In this study, a dual-head Nd: YAG pulsed laser (New Wave's SOLO III 15 HZ) has been used to provide a highly stable green light source to illuminate the PIV tracers at a 532 nm wavelength. The laser beam passed through two different sets of optical lenses, which were designed specifically, based on the laser

beam characteristics, to create a light sheet with an approximate thickness of 1 mm to illuminate the field of view. The PIV CCD camera was equipped with a Nikon Micro-NIKKOR 60 mm lens, and the lens aperture was kept open at  $f\# = 4$ . The field of view of the camera, for all cases, corresponded to a  $40 \times 30$  mm window with an approximate pixel size of  $6.5 \mu\text{m}$ . The images were then processed using LaVision DaVis 8.3 software to calculate the global instantaneous flow velocity field. This process was followed by a multi-pass spatial resolution improvement process with a decremental of the interrogation window size from  $32 \times 32$  to  $16 \times 16$  pixels, with a 75% overlap in the horizontal and the vertical directions. For each jet, a total of 750 images were acquired. By considering  $N = 750$  as the total number of images, time-averaged velocity vectors  $\langle u, v \rangle$ , in  $XZ$  plane were obtained from

$$\langle u, v \rangle = \frac{1}{N} \sum_{n=1}^N [u_n(x, z), v_n(x, z)] \quad (3)$$

It should be noted that for  $YZ$  plane measurements, similar equation can be used to calculate the time-averaged velocity components only by substituting 'x' index to 'y' index in Eq.3.

## 2.3 Concentration Measurements

Planar Laser Induced Fluorescence (PLIF) is a non-intrusive, spatially resolved laser diagnostic technique that has evolved into a valuable tool for the investigation of scalar flow fields. PLIF was developed and is most frequently used for the measurement of gas species concentrations. The PLIF relies on a pulsed laser sheet that illuminates a two-dimensional section of the flow field. The wave length of the laser sheet is tuned to excite the particular molecule, or atom, that is artificially seeded (e.g. acetone, biacetyl,  $\text{I}_2$ ) within the flow field. Typically, an ultraviolet wavelength is used to produce electronic excitation. A fraction of these excited molecules will emit a photon while simultaneously returning to the equilibrium state. This results in measurable fluorescence signals from the tracer and is thus captured by the CCD camera.

In this study, acetone vapor was mixed into air\helium at a consistent rate ( $\sim 20\%$ ) and was used as the tracer for concentration measurements. The intensified CCD camera was equipped with a Nikon Micro-NIKKOR 105 mm lens, the aperture was kept open at  $f\# 2.8$ , and a 378 nm UV bandpass filter with FWHM of 140 nm to capture the acetone fluorescence signal. The camera field of view for all cases corresponded to a  $38 \times 28$  mm window with an approximate pixel size of  $6.5 \mu\text{m}$ . Pulsed Nd: YAG laser (Spectra-Physics INDI-40-10-HG) has been used to provide the stable 266 nm wavelength UV light and excite acetone molecules. In order to be in the linear fluorescence regime, the laser beam passed through different sets of optical lenses, which were designed specifically, based on the laser beam characteristics, to create a light sheet with an approximate of height 5 cm and thickness  $350 \mu\text{m}$  at focus to illuminate the field of view.

In order to obtain pure fluorescence signal from raw PLIF images, one should take into accounts the uncertainties associated with background noise, laser beam intensity distribution, and laser energy fluctuations per pulse. For each experiment, the sets of background and laser sheet images were taken before and after the experiment to calculate the averaged background and cross-sectional laser beam intensity distributions. The laser sheet images provided all of the required information, regarding the spatial inhomogeneities of laser intensity and also the detection system's transmission errors. In order to consider the laser beams energy fluctuations, all images have been normalized by the laser energy, per pulse, which were obtained using a laser energy meter during the experiment. The images were then processed using LaVision DaVis 8.3 software to calculate the instantaneous concentration field. For each jet, a total of 750 images were acquired. The time-averaged concentration  $\langle c \rangle$  was thus calculated using

$$\langle c \rangle = \frac{1}{N} \sum_{n=1}^N [c(x, z)] \quad (4)$$

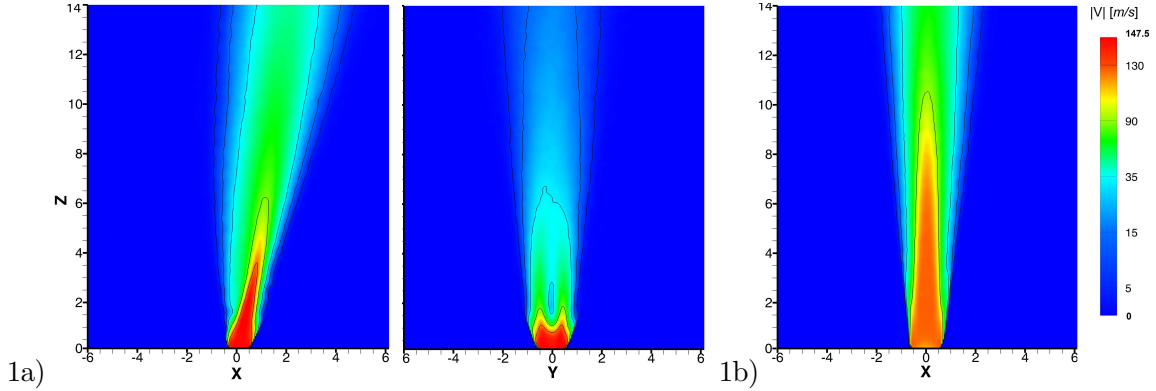
It should be noted that for  $YZ$  plane measurements, similar equation can be used to calculate the time-averaged concentration only by substituting ' $x$ ' index to ' $y$ ' index in Eq.4.

### 3.0 RESULTS

#### 3.1 Time-Averaged Flow Fields

The time-averaged velocity contours, obtained for all of the experiments conducted here, are shown in Fig. 2. These contours are shown in both the  $XZ$  and  $YZ$  planes for the jet emitting from the pipe experiments (3D jets), and only the  $XZ$  plane for the OP jets. Clearly, for the 3D jets in the  $XZ$  planes, for both gases, the jet is established with an asymmetric structure. There is a slight deviation from the vertical  $Z$ -axis in the direction of the initial flow inside the pipe. In this plane, significant jet spreading is observed as soon as the jets exit from the orifice. This spreading appears to be much more significant compared to the OP jet. Also, near the potential-core region, there is more jet spreading on the back side of the jet (left side) compared to the front. There is also a shorter potential-core length observed for helium compared to air. These potential core lengths, in the  $XZ$  planes, are approximately  $4D$  and  $5D$  for helium and air, respectively. The potential-core lengths of both gases are also shorter compared to the axi-symmetric OP jets. The respective core lengths of the OP jets for helium and air are  $7D$  and  $9D$ . In the  $YZ$  planes, for the 3D jet, the jet spreading appears to be more greater, compared to the  $XZ$  plane.

air:



helium:

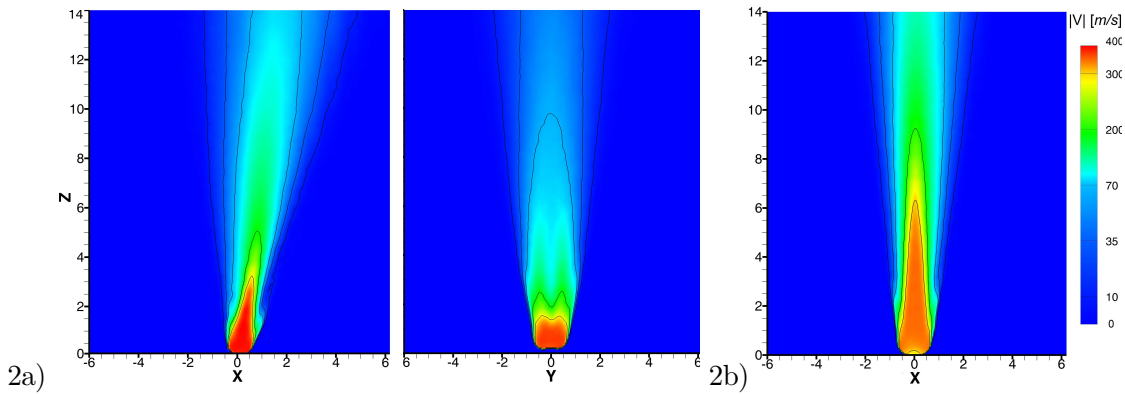
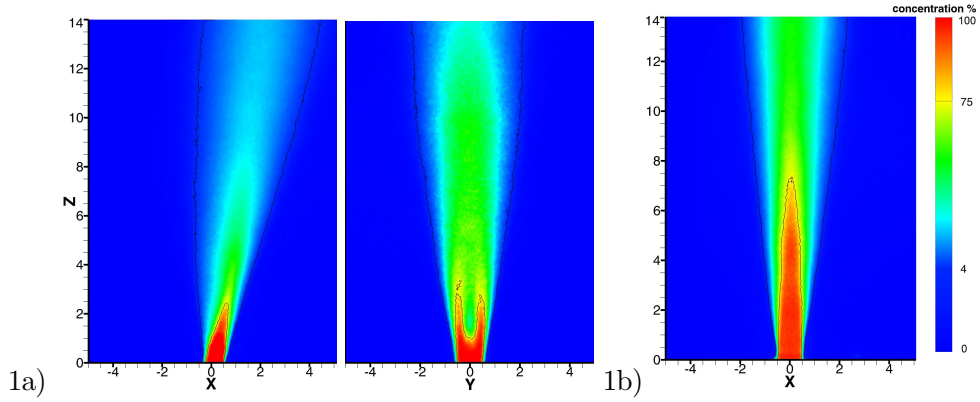


Figure 2: Average velocity contours in  $XZ$  and  $YZ$  planes for 1) air and 2) helium, obtained from a) Round jet on side of tube (3D jet) and b) Round orifice plate (OP) jet.

There are also two high-velocity peaks observed in this plane, for both gases, at  $Y \pm 0.5$ , on each side of the  $Z$ -axis, with a low-velocity region located on the axis at approximately  $Z = 2$ . These features are not observed in the OP jet. Also, the potential-core lengths in this plane are much shorter compared to the  $XZ$  plane. Here, the potential-core length for both gases is approximately  $1D$ . In general, it is observed that the helium and air jets have a qualitatively similar flow pattern for both the 3D jets and the OP jets. However, helium, in all cases, appears to have a faster velocity decay.

Figure 3 presents the time-averaged concentration contours of the 3D jets, in the  $XZ$  and  $YZ$  planes, and also the OP jets. In general, the concentration profiles are qualitatively similar to the velocity profiles presented in Fig. 2, with the exception of the helium 3D jet in the  $YZ$  plane. In this plane, the maximum concentration regions for helium, in the near field, follow the same pattern as velocity. Two maximum regions are observed at  $Y \pm 0.5$ , for both gases, with a concentration deficit on the  $Z$ -axis at  $Z = 2$ . However, beyond the near field, from  $Z > 4$ , the maximum concentration appears to be located on the  $Z$ -axis. Also, much higher concentration levels are observed beyond the near field compared to air, when  $3 > Z > 11$ . Finally, contours in Fig. 3 are shown for each gas at two specific concentrations by volume (4% & 75%) for the sake of discussion later on in this paper. These contours levels represent the hypothetical Lower Flammable Limit (LFL) and the Upper Flammable Limit (UFL) normally associated with hydrogen [10], respectively.

air:



helium:

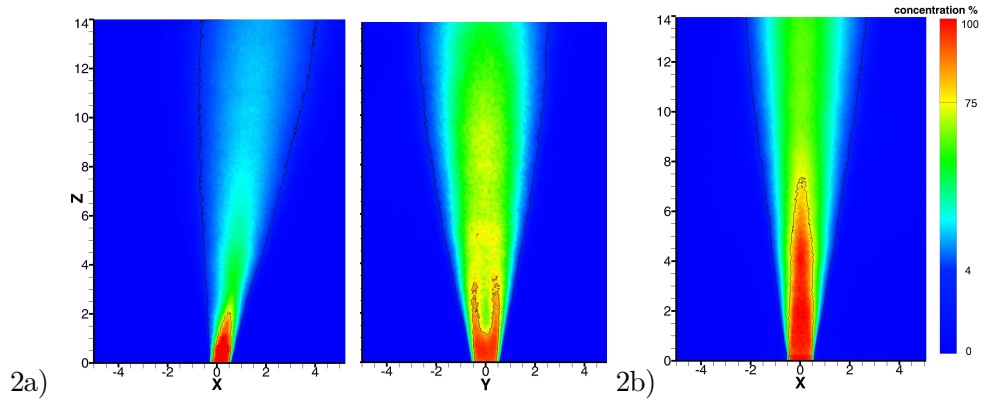


Figure 3: Average concentration contours in  $XZ$  and  $YZ$  planes for 1) air and 2) helium, obtained from a) 3D Round jet and b) Round orifice plate jet.

### 3.2 The Jet Centerline

As observed in the previous section, for the 3D jets in the  $XZ$  plane, the jet centerline always deviates from the  $Z$ -axis. In order to quantify this jet deflection, the trajectory of the jet was measured by locating the  $X$  coordinate corresponding to the maximum velocity magnitude ( $|\mathbf{V}|_{\max}$ ) at each downstream height from the orifice. These jet trajectories are shown in Fig. 4 for both helium and air in the  $XZ$  plane. Also shown are the corresponding locations of maximum concentration ( $|\mathbf{C}|_{\max}$ ). In general, both gases follow the same nearly linear trajectory from the orifice, up to  $Z \sim 4$ . From this point, a slight upward shift is noticeable for helium, whereas the air more or less continues to follow its original trajectory. Clearly, for these experiments, air deviates from the  $Z$ -axis more than the helium jet beyond the near field. For both gases, the centerlines were fit to power-law expressions using least-square regression and are also shown in the figure. The power-law expressions thus take the form of

$$Z = \beta_1 X^{\beta_2}, \quad (5)$$

where  $\beta_1$  and  $\beta_2$  are constants evaluated for each flow field accordingly. For air  $\beta_1 = 4.82$  and  $\beta_2 = 1.391$ , and for helium  $\beta_1 = 7.251$  and  $\beta_2 = 1.504$ . It was found that, for the range of heights considered here, the jet trajectories were well approximated by this power-law curve fit.

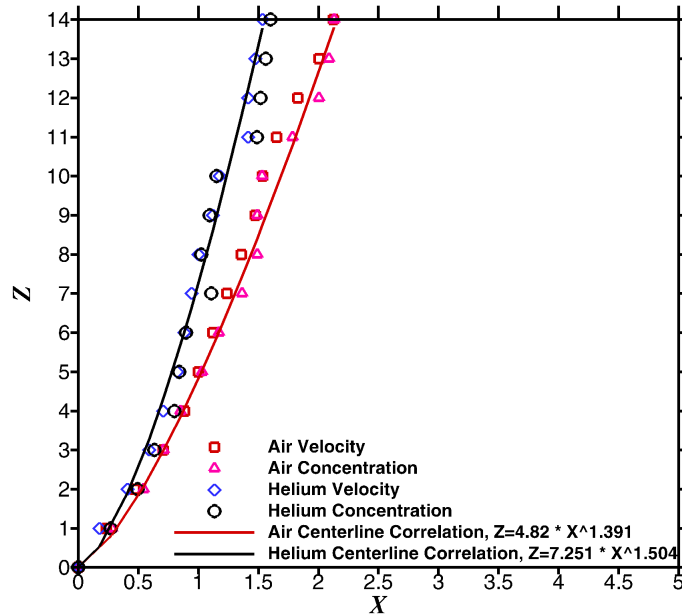


Figure 4: Jet centerlines taken along the location of maximum velocity ( $|\mathbf{V}|_{\max}$ ) locations.

### 3.3 Jet Centerline Properties

In order to characterize the jet flow in more detail, various properties were extracted along the jet centerlines. First, the inverse velocity decay for all cases are shown in Fig. 5a). For the OP jets, the velocity measurements along the centerline are straight forward. For the 3D jets, however, the velocity measurement, along the centerline, is obtained in both the  $XZ$  and  $YZ$  planes. In the  $XZ$  plane, the centerline velocities  $|\mathbf{V}|_c$ , as functions of  $Z$ , correspond to  $|\mathbf{V}|_{\max}$ , which were determined in the previous section. In the  $YZ$  plane, owing to symmetry, the centerline velocity  $|\mathbf{V}|_c$  is simply measured along the

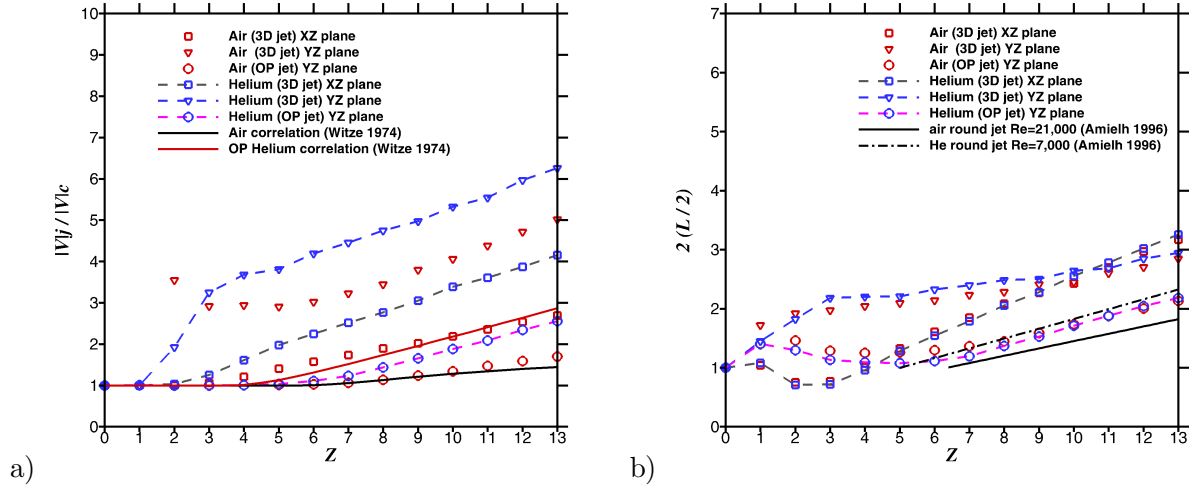


Figure 5: a) Jet inverse velocity decay and b) jet widths ( $2(L/2)$ ) obtained along the  $|\mathbf{V}|_c$  centerlines

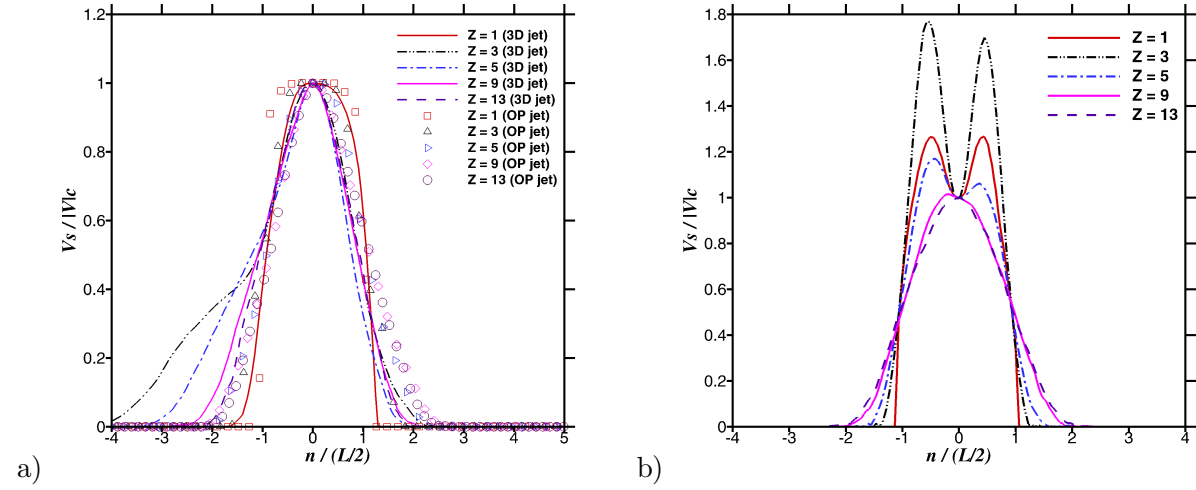
$Z$ -axis at  $Y = 0$ . Also, for comparison, round jet correlations of Witze [11] for air and helium, at the corresponding conditions, are presented. These correlations were determined from dozens of subsonic and supersonic jet experiments, all having different fluid densities. For both gases, the OP jets match well with the Witze correlations [11]. The helium jet velocity is found to decay faster than air, as observed by the steeper slope in the Fig. 5a). Also, the potential-core length of helium was slightly shorter compared to air. For the OP jets, the potential core lengths of helium and air are  $Z = 5$  and  $Z = 7$ , respectively. For the 3D jet velocity decays, in the  $XZ$  plane, both gases are found to decay much faster than in their corresponding OP jet experiment. Although the same trend is observed, where helium velocity decays faster than air, the potential-core lengths for helium and air are found to be  $Z = 2$  and  $Z = 3$ , respectively. Finally, the 3D jets, in the  $YZ$  planes, were found to have a faster velocity decay compared to the  $XZ$  plane and OP experiments. It is noted, however, that the true jet centerline is in fact on the  $XZ$  plane. It is also worth noting that, in the  $YZ$  plane, air velocity initially decays faster than helium in the near field, when  $Z < 2$ .

Next, Fig. 5b) shows the downstream evolution of the jet widths,  $2(L/2)$ , for each experiment. For the OP jet, the jet width is simply determined by the locations normal to the jet centerline (along  $Y$ ) where  $|\mathbf{V}| = 0.5|\mathbf{V}|_c$  at any given location along  $Z$ . For the 3D jet in the  $XZ$  plane, however, the centerline and the corresponding normal do not correspond to  $Z$ , or  $X$ . Instead, the downstream distance,  $s$ , was measured along the jet centerline, and  $n$  was defined as the vector normal to it. The  $(s, n)$  coordinate system is related to the Cartesian coordinate system by rotating the  $(X, Z)$  plane through the angle  $\alpha$  about  $Z$ -axis, as illustrated previously in Fig. 1. In the  $YZ$  plane, the  $n$  component corresponds to the  $Y$  direction due to symmetry. Also shown in the Fig. 5b) are the jet widths determined previously for several round jet experiments [12]. The OP jets were found to have nearly constant jet widths up until  $Z \sim 5$ . From this point on, the jet spread was found to increase linearly, consistent with the previous experimental studies. For the 3D jets, in the  $XZ$  plane, a similar trend was observed. However, both gases experience a slight contraction in jet width between  $1 < Z < 4$ . Beyond this point, the jet spreading is observed to be much greater compared to the OP jets. In the  $YZ$  plane, the 3D jets are found to spread significantly in the near field, starting from the orifice location. Eventually, in the far field, the spreading rates are comparable to those observed in the  $XZ$  plane. In all cases, the spreading rates of helium are found to be consistent with air.



Additionally, the velocity profiles for both gases are presented in Fig. 6 at several downstream locations along the jet centerline coordinate,  $s$ . The  $s$ -component velocities, shown, are normalized by the local centerline velocity magnitudes ( $|V|_c$ ). Also, the  $n$  coordinate, which is normal to the centerline curve  $s$ , is normalized by the jet half widths ( $L/2$ ), determined from Fig. 5b. For the OP jets, a semi top-hat profile is observed near the orifice location (at  $Z = 1$ ), as expected. This profile later develops into a self similar, Gaussian-like shape after  $Z > 5$  for both gases. This behavior is typical of axis-symmetric round jets [6]. For the 3D jets, on the  $XZ$  plane, the velocity profiles generally compare well to the OP jets. In fact the profiles match well for both gases in the  $-1 < (n/(L/2)) < 1$  region for all  $Z$  locations. Discrepancies between the 3D jets and the OP jets are observed, however, beyond this range, on the outer edges of the jet. In fact, it is observed that the 3D jets are more diffusive on the back side of the jet (shown in  $-n$  direction) compared to the OP counter parts. This was previously observed in Fig. 2. Only in the far field, when  $Z > 9$ , the 3D jet profiles match the OP profiles.

air:



helium:

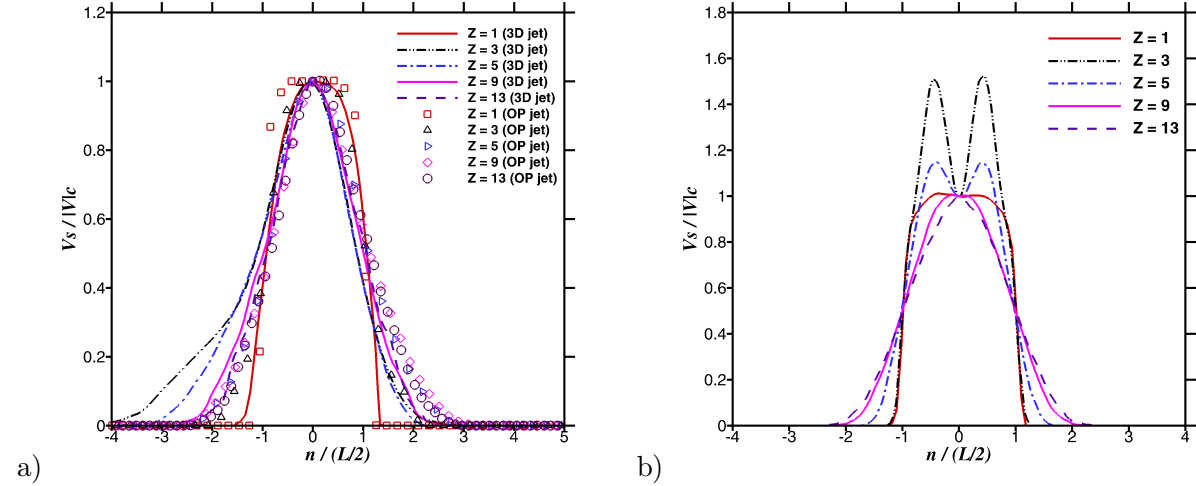


Figure 6: Average velocity profiles, along jet centerlines, taken at various heights for air and helium, obtained from a) OP & 3D jet in  $XZ$  plane and b) 3D jet in  $YZ$  planes.

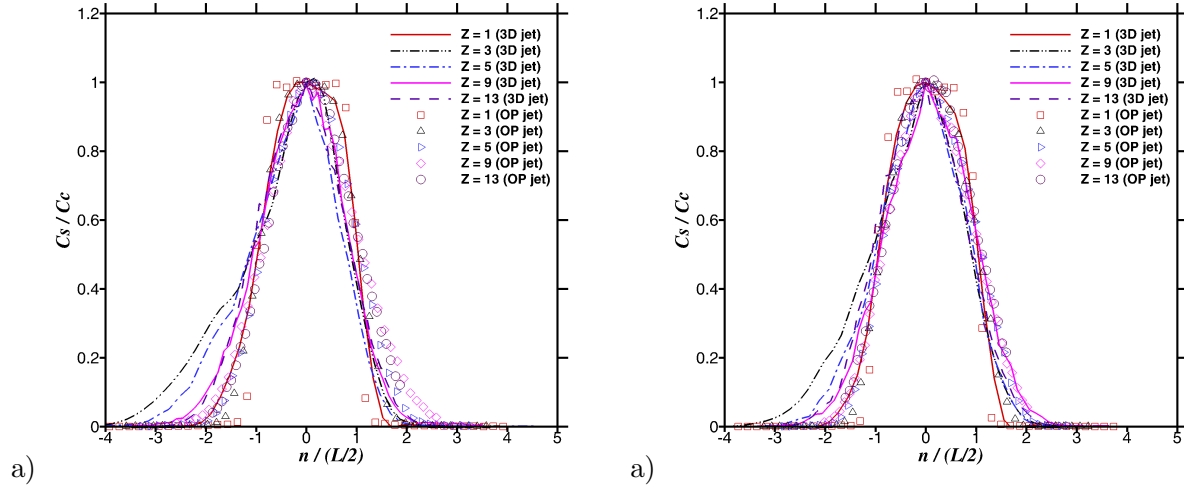


Figure 7: Average concentration profiles, along jet centerlines, taken at various heights for a) air and b) helium, obtained from OP & 3D jet in  $XZ$  plane.

In the  $YZ$  plane of the 3D jet, a very different jet evolution is observed. Here, a saddle-back velocity profile is observed for both gases, which is similar to previous axi-symmetric sharp-edged inflow jet studies [7]. This profile confirms earlier observations, in Fig. 2, of the jet having two high velocity regions in the near field ( $Z < 9$ ), at  $(n/(L/2)) \pm 0.5$ , with a low velocity region centered on the  $Z$ -axis at  $n = 0$ . Finally, in all cases, the velocity profiles for helium and air were found to be qualitatively similar to each other.

Finally, the radial concentration profiles for both gases along the jet centerlines coordinate ( $s$ ), only for the OP jets and the 3D jets in the  $XZ$  plane, are shown in Fig.7. The radial concentrations  $C_s$ , shown here, are normalized by the local centerline concentrations ( $C_c$ ). They were found to be qualitative similar to the velocity profiles in all cases.

## 4.0 DISCUSSION

For the 3D jets, asymmetric flow structure was always observed. It was found that the perpendicular nature of the orifice, relative to the direction of flow within the pipe, causes a deflection of the jet away from the vertical axis. It is not yet clear how the deflection angles scale for each gas, however, air is found to deflect more than helium, despite having equal initial momentum flux (force) ejecting through the orifice. Initially, from Fig. 4, both gases have very close deflection angles. Thus, buoyancy is probably the dominant factor which causes helium to deflect less than air in the far field.

Further asymmetry was observed in the 3D jet when comparing the  $XZ$  planes to the  $YZ$  planes in Figs. 2 and 6. In the  $YZ$  plane, saddle-back behavior is observed in both the velocity and concentration profiles. In this sense, maximums were found to exist roughly  $Y \pm 0.5$  away from the  $Z$ -axis, with a velocity deficit located on the axis, at a height of  $Z = 2$  for both gases. This could be due to the well-known vena contracta effect, generated immediately downstream from the orifice, and therefore an inward radial velocity exits at the edge of the jet[13]. A corresponding numerical investigation [14] has revealed that this feature is also caused by vortex shedding within the orifice as the flow within the pipe suddenly emerges through the orifice. There may also be large scale vortex patterns contributing to this saddle-back profile, as was reported to be the case in axi-symmetric elliptical jets [15, 16]. However, this

remains to be investigated.

In terms of jet spreading along the centerline, the 3D jets (in the  $XZ$  plane) were found, from Fig. 5b, to spread much more compared to the OP jets. Also, from the jet spreading in the  $YZ$  planes of the 3D jets, spreading occurs immediately from the orifice. In fact, Figs. 2 and 6 have revealed that the 3D jet experiences more asymmetric jet spreading on the back side of the jet, especially in the near field. All of this suggests that there is much more turbulent mixing in the 3D jets compared to the OP jets. This would, in turn, explain the shortening of the potential-core lengths as observed in the velocity decay profiles of Fig. 5a. It is well known that turbulent mixing rates can reduce the potential-core length of a jet [17]. This enhanced turbulent mixing would also explain why the 3D jets were observed to decay faster than the OP jets.

In general, velocity and concentration decays are always faster in helium compared to air, for both the OP and 3D jets. This behavior matches the trends according to the correlations of Witze [11], which take into account the density and Mach number of the jet. Lighter and faster jets are thus observed to decay more rapidly than heavier and slower jets. Furthermore, while the OP jets were found to correlate well with Witze, it was found that such correlations do not accurately determine the velocity decay of the realistic 3D pipe and orifice configuration considered here.

Finally, concentration contours were presented in Fig. 3. Helium was found to have much higher concentration levels beyond the near field compared to air, when  $3 > Z > 11$ . This is probably attributed to low Schmidt numbers ( $Sc < 1$ ), i.e. mass diffusion rates are faster than momentum diffusion. Without considering difference in diffusivity between helium and hydrogen, the helium experiments conducted here served to provide the insight into how the ignition limits in hydrogen might evolve, qualitatively. However detailed numerical simulations are required to safely and accurately determine such ignition limits for hydrogen. This avenue is currently being pursued [14] by taking into account the experimental data from here as validation. However, due to unsteady nature of the jet, as observed from instantaneous concentration fields (not shown here) and other studies[18], a number of occasional spikes of gas concentration above the flammability margin occur even if the mean concentration remain below the margin. Therefore, not only time-averaged concentration fields but also transient fields must be taken into account, in order to establish proper safety thresholds for the sudden release of hydrogen.

## 5.0 CONCLUSIONS

Here, experiments were conducted in order to investigate compressible turbulent jets, of varying gas densities and Reynolds numbers, issuing from realistic pipe geometry, and compared to axi-symmetric round jets. It was found that flow within a pipe, perpendicular to an upward facing hole, causes the resulting jet to deflect at an angle relative to the vertical axis, in the direction of the pipe itself. In general, both air and helium were found experience much more jet spreading compared to the axi-symmetric jet experiments. Also, more jet spreading was observed on the back side of the asymmetric 3D jet compared to the axi-symmetric case. This enhanced mixing in the asymmetric case caused a reduction in the potential-core length, and an increase in the velocity decay rate. As a result, round jet assumptions do not accurately describe the correct dispersion and velocity decay rates of jets issuing from realistic geometries. Finally, hypothetical ‘ignition limits’ were determined for helium, which are indicative of how hydrogen dispersion may behave in the realistic pipe configuration considered here.

The authors would like to acknowledge funding from the Natural Sciences and Engineering Research Council of Canada (NSERC).

## 6.0 REFERENCES

1. Wagnanski, I. and Fiedler, H., Some measurements in the self-preserving jet, *Journal of Fluid Mechanics*, **38**, no. 03, (1969), pp. 577–612, URL <http://dx.doi.org/10.1017/S0022112069000358>.

2. Panchapakesan, N.R. and Lumley, J.L., Turbulence measurements in axisymmetric jets of air and helium. Part 2. Helium jet, *Journal of Fluid Mechanics*, **246**, (1993), pp. 225–247, URL <http://dx.doi.org/10.1017/S0022112093000102>.
3. Pitts, W.M., Effects of global density ratio on the centerline mixing behavior of axisymmetric turbulent jets, *Experiments in Fluids*, **11**, no. 2, (1991), pp. 125–134, URL <http://dx.doi.org/10.1007/BF00190288>.
4. Pitts, W.M., Reynolds number effects on the mixing behavior of axisymmetric turbulent jets, *Experiments in Fluids*, **11**, no. 2, (1991), pp. 135–141, URL <http://dx.doi.org/10.1007/BF00190289>.
5. MI, J., NOBES, D.S. and NATHAN, G.J., Influence of jet exit conditions on the passive scalar field of an axisymmetric free jet, *Journal of Fluid Mechanics*, **432**, (2001), pp. 91–125, URL <http://dx.doi.org/10.1017/S0022112000003384>.
6. Mi, J., Kalt, P., Nathan, G.J. and Wong, C.Y., PIV measurements of a turbulent jet issuing from round sharp-edged plate, *Experiments in Fluids*, **42**, no. 4, (2007), pp. 625–637, URL <http://dx.doi.org/10.1007/s00348-007-0271-9>.
7. Quinn, W.R., Upstream nozzle shaping effects on near field flow in round turbulent free jets, *European Journal of Mechanics - B/Fluids*, **25**, no. 3, (2006), pp. 279–301, URL <http://www.sciencedirect.com/science/article/pii/S0997754605000993>.
8. Chen, C.J. and Rodi, W., Vertical turbulent buoyant jets : a review of experimental data, Pergamon Press, Oxford; New York, 1980.
9. McBride, B.J., Gordon, S. and Reno, M.A., Coefficients for calculating thermodynamic and transport properties of individual species, Technical report, 1993.
10. Coward, H.F. and Jones, G.W., Limits of flammability of gases and vapors. Pittsburgh, PA: US Department of the Interior, Bureau of Mines, *Bulletin*, **503**.
11. Witze, P.O., Centerline Velocity Decay of Compressible Free Jets, *AIAA Journal*, **12**, (1974), pp. 417–418, doi:10.2514/3.49262.
12. Amielh, M., Djeridane, T., Anselmet, F. and Fulachier, L., Velocity near-field of variable density turbulent jets, *International Journal of Heat and Mass Transfer*, **39**, no. 10, (1996), pp. 2149–2164, URL <http://www.sciencedirect.com/science/article/pii/0017931095002944>.
13. Mi, J., Nathan, G.J. and Nobes, D.S., Mixing Characteristics of Axisymmetric Free Jets From a Contoured Nozzle, an Orifice Plate and a Pipe, *Journal of Fluids Engineering*, **123**, no. 4, (2001), pp. 878–883, doi:10.1115/1.1412460, URL <http://dx.doi.org/10.1115/1.1412460>.
14. Maxwell, B., Soleimani nia, M., Oshkai, P. and Djilali, N., Large eddy simulations of asymmetric turbulent hydrogen jets issuing from realistic pipe geometries, Proceedings of the 7th International Conference on Hydrogen Safety, Hamburg, Germany.
15. Quinn, W.R., Experimental study of the near field and transition region of a free jet issuing from a sharp-edged elliptic orifice plate, *European Journal of Mechanics - B/Fluids*, **26**, no. 4, (2007), pp. 583–614, URL <http://www.sciencedirect.com/science/article/pii/S0997754606001142>.
16. Hussain, F. and Husain, H.S., Elliptic jets. Part 1. Characteristics of unexcited and excited jets, *Journal of Fluid Mechanics*, **208**, (1989), pp. 257–320, URL <http://dx.doi.org/10.1017/S0022112089002843>.
17. Zaman, K.B.M.Q., Asymptotic spreading rate of initially compressible jets-experiment and analysis, *Physics of Fluids*, **10**, no. 10, (1998), pp. 2652–2660, doi:10.1063/1.869778, URL <http://dx.doi.org/10.1063/1.869778>.
18. Chernyavsky, B., Wu, T.C., Pèneau, F., Bènard, P., Oshkai, P. and Djilali, N., Numerical and experimental investigation of buoyant gas release: Application to hydrogen jets, *International Journal of Hydrogen Energy*, **36**, no. 3, (2011), pp. 2645–2655, URL <http://www.sciencedirect.com/science/article/pii/S0360319910008323>.